Orientation dependence of dynamic compared to static recovery in Interstitial Free steel

Sepúlveda Hernández, Estefanía; Nguyen-Minh, Tuan; Traka, Konstantina; Castro Cerda, Felipe; Kestens, Leo A.I.

DOI
10.1016/j.scriptamat.2024.116151

Publication date
2024

Document Version
Final published version

Published in
Scripta Materialia

Scripta Materialia 249 (2024) 116151

Contents lists available at ScienceDirect

Scripta Materialia

journal homepage: www.journals.elsevier.com/scripta-materialia

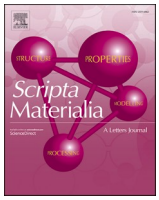

Orientation dependence of dynamic compared to static recovery in Interstitial Free steel

Estefanía Sepúlveda Hernández [a,b,*], Tuan Nguyen-Minh [a], Konstantina Traka [c], Felipe Castro Cerda [b], Leo A.I. Kestens [a,c]

[a] Department of Electromechanical, Systems and Metal Engineering, Ghent University, Ghent, Belgium
[b] Department of Metallurgical Engineering, Universidad de Santiago de Chile, Estacion Central, Chile
[c] Department of Materials Science and Engineering, Delft University of Technology, CD, Delft 2628, the Netherlands

ARTICLE INFO

Keywords:
Misorientation gradient
Recovery
Crystallographic texture
IF steel

ABSTRACT

This study investigates the sub-structure of IF steel in three conditions: cold rolled, statically recovered, and warm rolled. After both cold and warm rolling, the steel exhibits the typical ⟨110⟩//RD and ⟨111⟩//ND fiber textures. Considering the short-range misorientation gradient $\Delta\theta/\Delta x$ to assess locally stored energy variations, it was observed that ⟨111⟩//ND grains exhibit significantly higher gradients than ⟨001⟩//ND grains in all conditions. In the statically recovered conditions, the $\Delta\theta/\Delta x$ values are significantly reduced compared to the cold rolled condition, but these values are significantly higher than those of the dynamically recovered after warm rolling. The strongly reduced orientation gradients in the ⟨111⟩//ND grains after warm rolling may reduce the nucleation potency of these orientations in the ensuing recrystallization. This study enhances our knowledge of deformation microstructure as a function of rolling temperature and is relevant in explaining reported differences in annealing textures during static recrystallization after cold vs warm rolling.

Most metallic alloys accommodate plastic deformation by dislocation slip [1,2]. Because of the imposed boundary conditions, the plastic displacement field will generally give rise to a combination of plastic strain and rigid body rotation. The difference between rigid body spin $\dot{\beta}$ and plastic spin $\dot{\omega}$ will give rise to a crystal lattice spin $\dot{\Omega}$ which, in turn, produces a deformation texture in a polycrystalline aggregate [3]. The rolling deformation texture of body centered cubic (BCC) materials, like low carbon steel, is generally composed of the α-(⟨110⟩//RD) and the γ-(⟨111⟩//ND) fiber texture components. This deformation texture is well-known for cold rolled samples, but it has also been observed in warm rolled samples [4–6], for which the rolling temperature is lower than the ferrite-austenite phase transformation temperature but high enough to facilitate thermally activated processes (typically at $\gtrsim T_m[K]/3$). Though cold and warm rolling produces similar deformation textures, the texture evolution after recrystallization annealing may be sharply different. The recrystallization texture of cold-rolled samples is commonly characterized by the γ-fiber, with the highest intensity on the {111}⟨112⟩ component, while annealing textures of warm-rolled samples conventionally contain components of the θ-(⟨001⟩//ND) fiber, with the maximum intensity peak near the {001}⟨110⟩ component [7,8]. Previous studies [5,8–10] have mentioned that the substructures generated by cold or warm rolling exhibit significant variations between grains of different orientations, which may be related to the observed variations in recrystallization texture. This study complements previous research by measuring and observing structural differences in the microstructures of warm and cold rolled samples. These differences are attributed to dislocation structures, quantified by the misorientation gradients gauged by the EBSD technique. It is not expected that the microstructural variations are due to the presence or absence of dynamic strain aging, as observed in previous studies [8], because the present material under investigation is IF steel with virtual absence of interstitial solutes in the iron matrix.

From stage III onward of the plastic flow curve, competing mechanisms of strain hardening and softening dominate the plastic response to the externally applied load [11–13]. The essential difference between cold and warm deformation is the fact that beyond a certain critical temperature, the softening mechanisms are thermally activated within the given time frame allowed for by the imposed strain rate $\dot{\varepsilon}$ and even further enhanced by the applied load. According to Gilbert et al. [14] the dislocation velocity under an applied load of ~100 MPa is increased

* Corresponding author.
E-mail address: Estefania.sepulvedahernandez@ugent.be (E. Sepúlveda Hernández).

https://doi.org/10.1016/j.scriptamat.2024.116151
Received 12 January 2024; Received in revised form 15 April 2024; Accepted 23 April 2024
Available online 30 April 2024

with one order of magnitude by increasing the deformation temperature from 300 to 500 K, which will affect the mean free path $\langle\lambda\rangle$ of dislocations. An increased dislocation velocity can accommodate a larger fraction of the strain rate and therefore the dislocation generation rate $\dot{\rho}$, required to sustain the imposed strain rate, can be reduced resulting in an increased mean free path $\langle\lambda\rangle$ ($\sim 1/\sqrt{\rho}$) [13,15,16]. Moreover, thermal activation will increase the annihilation rate of dislocation dipoles, which equally contributes to a reduction of (immobile) dislocations and therefore will lead to a coarser deformation substructure. In general, these mechanisms are well documented in the literature [11,13,16,17], though the associated orientation dependence of dynamic recovery is not yet described in detail. The present paper aims to address this knowledge gap by analyzing the crystal orientation maps of the dynamically recovered state (after warm rolling) and comparing it to the reference state after cold rolling and/or static recovery.

The studied material is an Interstitial Free (IF) steel with the chemical composition listed in Table 1. The as-received state of this material is a hot rolled sheet of 3.5 mm thickness. One strip of this hot-rolled material was cold rolled in various passes to reduce the strip thickness by 80 % on a two-high laboratory rolling mill with roll diameters of 350 mm. Another strip of the initial material was first reheated to 550 °C for 1,800 s and then rolled by a single pass of 80 % thickness reduction immediately after retracting from the furnace. The warm rolled sample will be in a dynamically recovered condition.

A cold rolled strip of 400 mm length and 25 mm width was submitted to a gradient annealing treatment whereby one end of the sample was submerged in a salt-bath furnace for 120 s and the other end of the sample was clamped in a solid copper block at room temperature. Temperature measurement by welded thermocouples along the strip length revealed a temperature of 900 °C for the sample end submerged in the furnace, and 60 °C for the sample end attached to the copper block. By microstructural characterization, it was observed that the annealed sample has evolved from 0 % to 100 % recrystallized volume fraction over a distance of ~40 mm starting from the furnace submerged end peeking out above the liquid salt surface. In the present study, a specific segment of the annealed strip was investigated that has reached a temperature of 600 °C, which was the last segment preceding the onset of recrystallization and therefore was in a statically recovered state.

EBSD (Electron Backscatter Diffraction) measurements were carried out with an FEI Quanta™ 450-FEG-SEM equipped with a Hikari EBSD camera. Samples for EBSD characterization were prepared by conventional grinding, polishing, and electropolishing steps. Additionally, a limited number of samples were prepared for TKD (Transmission Kikuchi Diffraction) with the conventional TEM (Transmission electron microscopy) sample preparation procedure [18]. The scanning electron microscope (SEM) was operated at an accelerating voltage of 20 kV and a beam current of 2.3 nA. The number of points for each scan is around 600,000 in an area of 102 × 52 μm^2 with a step size of 0.1 μm and a square scanning grid pattern. The post-processing of the data was carried out with OIM™ Software version 8.2. [19].

To estimate the local stored energy, a variety of EBSD-based metrics can be used [20–22]. In general, these metrics can be divided in grain-based and (local) kernel-based types. The grain-based metrics require the specification of the maximum allowed tolerance to define a grain, which is an operator-based criterion and arbitrary to some extent. Alternatively, in the present work, a kernel-based metric will be used. The most common kernel-based parameter is the KAM value (i.e. the average disorientation of the kernel central point with respect to its neighbors), which critically depends on the number of nearest neighbors that are considered. Moussa et al. [23,24] and Lanjewar et al. [25] have shown that the arbitrary choice of a number of nearest neighbors can be avoided by considering the KAM slope, i.e. for each pixel the slope ($\Delta\theta/\Delta x$) of the linear increase of KAM as a function of several nearest neighbors is considered as a metric for stored energy of plastic deformation. The dimension of this slope is deg/μm, corresponding to the dimension of the elements of Nye's curvature tensor, of which the magnitude determines the density of geometrically necessary dislocations (GNDs) [26,27]. It is less accurate to consider the KAM value to evaluate the dislocation density as Pantleon [26] reports how the curvature tensor is positively related to the dislocation density, which on the mere basis of dimension control favors the consideration of misorientation gradient as a measure of stored energy.

The determination of local stored energy through EBSD is contingent on the angular resolution of the measurements [28] . However, the angular resolution is influenced by various parameters that introduce dispersion in the measured orientation around the true orientation, essentially constituting noise. Enhancing the quality of the data involves post-processing aimed at reducing this dispersion between the measured and true values through averaging, allowing to accurately identify regions with genuine differences in orientation. A filtering approach of this nature was proposed by Kuwahara [29] and will be applied here in post-processing the orientation scans.

Fig. 1. shows the microstructure maps color-coded by inverse pole figure (IPF) along the normal direction (ND) of the material after cold rolling, static recovery, and dynamic recovery. The static and dynamic recovery samples contained a small volume fraction of recrystallized grains (~ 15 %) that were filtered out of the data set by applying a grain orientation spread (GOS) threshold of 1.5° [30–32] (i.e. all grains with GOS < 1.5° were considered as recrystallized). The recrystallized grains appear as white areas in Fig. 1b and c. The microstructural evolution during plastic deformation of low carbon steels is quite different between so-called Taylor hard grains, i.e., ⟨111⟩//ND orientations, and Taylor soft grains, i.e., ⟨001⟩//ND [10,33]. Therefore, Fig. 1d-f and Fig. 1g-i display ⟨001⟩//ND (red grains) and ⟨111⟩//ND (blue grains) separately with an angular tolerance of 20°

Fig. 1k and Fig. 1l show the low-angle grain boundaries (LAGB) of the cold rolled and annealed sample at 600 °C (i.e. the statically recovered) and the warm rolled sample (i.e. dynamically recovered). From Fig. 1j it can be observed that in the statically recovered condition, the cell size is independent of the angular tolerance; conversely, the dynamically recovered structure exhibits an increase of the average cell size with increasing angular tolerance, which implies that the statically recovered state exhibits a more fragmented (sub-)structure with a smaller cell size as compared to the dynamically recovered state. In the dynamically recovered condition, Fig. 1l, not all cells surrounded by LAGBs carrying a disorientation of 1, 2 or 3° are fully "closed" whereas in the statically recovered state (Fig. 1k) most of the cells are fully surrounded (i.e. "closed") by LAGBs with disorientations of not larger than ~2°

Several studies indicate that the texture of warm-rolled sheet very much resembles the one of cold-rolled sheet [6,34,35]. Fig. 2 shows the texture of (a) the cold rolled, (b) the statically recovered, and (c) the dynamically recovered sample after warm rolling. EBSD measurements for texture analysis were performed with a step size of 0.4 μm in an area of 768 μm x 768 μm and all pixels corresponding to recrystallized grains were excluded from the texture calculation. The textures are characterized by a strong α- and γ-fiber. Generally, heat activation induces both recovery and recrystallization processes; however, only the latter entails the migration of high-angle boundaries, thereby altering the crystallographic texture [17]. While the statically annealed sample was anticipated to exhibit no recrystallization, it has nonetheless manifested to a certain degree, resulting in a partial modification of the crystallographic texture. The strongest component after cold rolling and static recovery is {112}⟨110⟩ while after warm rolling it is {111}⟨112⟩. The alteration in peak intensity observed in the γ-fiber, transitioning from {111} ⟨112⟩

Table. 1
Chemical composition of IF steel (wt %).

C	Mn	Al	N	Ti
0.002	0.095	0.05	0.002	0.045

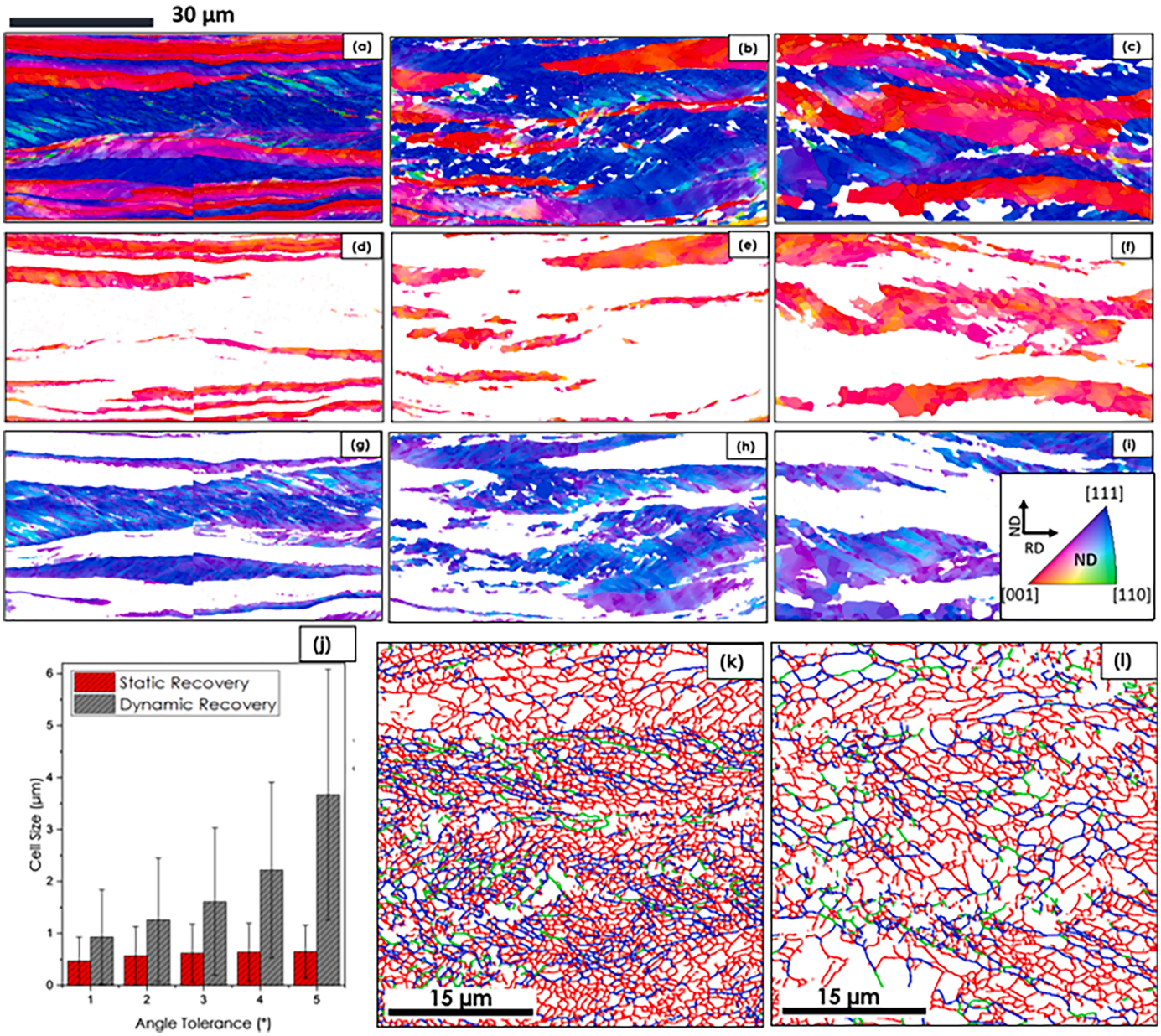

Fig. 1. ND-IPF maps of IF Steel (a) 80 % cold rolled full hard condition (b) statically recovered and (c) warm rolled 80 % (dynamically recovered). ⟨001⟩//ND-IPF maps with tolerance of ±20° of (d) 80 % cold deformed (e) statically recovered (f) and warm rolled sample (dynamically recovered). (g), (h), (i) show the corresponding ND-IPF maps for the ⟨111⟩//ND grains with a tolerance of ±20° (j) Cell size versus tolerance angle for statically and dynamically recovered state. Grain boundary maps samples after (k) static recovery and (l) after dynamic recovery. Boundaries in green 10°–15°, blue color 5°–10°, and red 1°–5° misorientation.

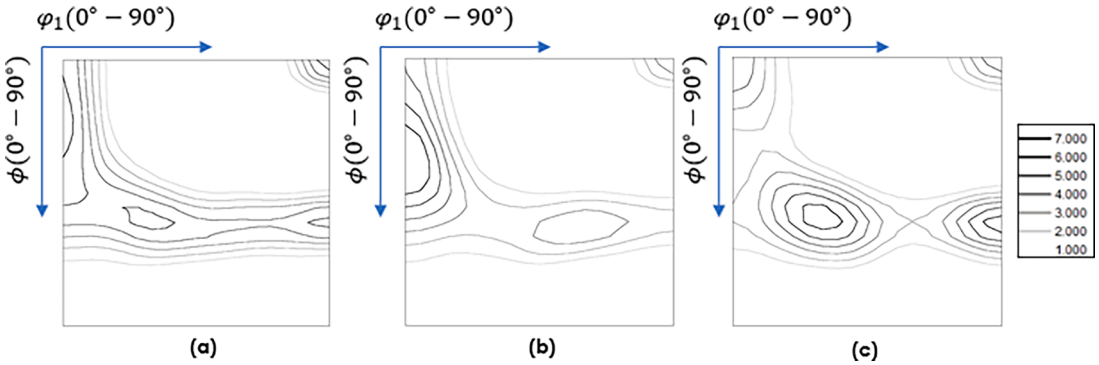

Fig. 2. $\varphi_2 = 45^\circ$ section of the orientation distribution function (ODF) of IF steel after (a) cold rolling (b) static recovery annealing and (c) warm rolling (dynamically recovered). ODFs were derived by Gaussian superposition with a spread of 5°.

after cold rolling (Fig. 2a) to {111}⟨110⟩ after static recovery (Fig. 2b), can be attributed to the recrystallization process, leading to the formation of new grains within the microstructure. Notably, there is a preference for the {111}⟨112⟩ component during recrystallization resulting in a diminished intensity of this component in the static recovery texture. The fact that a minor fraction (~15 %) of recrystallized grains is removed from the data set does not affect the conclusions.

The misorientation gradient Δθ/Δx was calculated with the kernel average misorientation data collected for 1 to 3 neighbors for an EBSD scan that was recorded with a step size of 0.1 μm and smoothed with a Kuwahara noise filter. The present KAM analysis considers three nearest neighbors, which corresponds to a distance of 0.2 μm, taking into consideration that from the 4th nearest neighbor onwards the slope starts to decay, as was expected based on literature reports [36,37]. The accumulated frequency distribution of the misorientation gradient is presented in Fig. 3. It can be observed that the cold rolled sample exhibits the steeper evolution of the accumulative misorientation gradient, decreasing after static recovery and warm rolling. It indicates that the misorientation gradients Δθ/Δx are strongest in the cold rolled sample, weakest in the dynamically recovered material, and intermediate in the statically recovered sheet. The mean misorientation value can be related to the density of GNDs [23–25], which is a statistical parameter reflecting the density of virtual dislocations contributing to the non-zero part of the accumulated Burgers vector for an arbitrary Burgers circuit of representative microstructural size. If the implicit assumption is made that the GND density is proportional to the overall dislocation density, it can be surmised that the measured local orientation gradient is an acceptable measure for the stored energy of plastic deformation. The higher value of the mean misorientation gradient is related to higher stored energy in the system (in this case, the mode of the frequency distribution is shown in Fig. 3b). However, an estimation of the absolute density of GNDs and the associated energy from the orientation gradients cannot be made unless making several critical assumptions on the type of dislocations and their configuration. Therefore, in the present study, only the orientation gradients will be considered.

The data of Table 2 reveals distinctive features in the substructure between static and dynamic recovery processes. Analysis of the misorientation gradients reveals significant variations, with cold-rolled samples exhibiting the highest values, followed by static and dynamic recovery. Specifically, the mode of the misorientation gradient for cold-rolled samples is 2.92 °/μm, while static and dynamic recovery exhibit values of 1.68 and 0.87 °/μm, respectively. It is observed that the gap in the mode values for ⟨111⟩//ND and ⟨001⟩//ND grains narrows during dynamic recovery compared to the statically recovered, though the standard deviation for ⟨111⟩//ND grains remains significantly larger (~15 %) as compared to the ⟨001⟩//ND grains, which may be instrumental in selecting ⟨001⟩//ND grains for recrystallization. In the dynamic recovery state, both ⟨111⟩//ND and ⟨001⟩//ND grains experience a drop of more than 55 % in the Δθ/Δx mode value compared to the cold rolled full hard state. Though in the statically recovered conditions, the Δθ/Δx values are reduced compared to the cold rolled condition, nevertheless, they remain ~40 % and ~30 % larger for the ⟨111⟩//ND and ⟨001⟩//ND grains, respectively, as compared to the dynamically recovered condition. Lastly, there is a disparity in the development of LAGBs between static and dynamic recovery, attributed to the difference in the kinetics of mechanisms involved in both recoveries (see below).

Table. 2
Misorientation gradient distribution mode and standard deviation (°/μm) of cold rolling, static recovery, and dynamic recovery.

		Mode Misorientation Gradient (°/μm)	Standard Deviation (°/μm)
Cold Rolling	⟨111⟩// ND	2.12	7.63
	⟨001⟩// ND	1.98	6.13
Static Recovery	⟨111⟩// ND	1.70 (−20 %)	6.03
	⟨001⟩// ND	1.51 (−24 %)	5.26
Dynamic Recovery	⟨111⟩// ND	0.82 (−61 %)	5.05
	⟨001⟩// ND	0.83 (−58 %)	4.44

The accumulated frequency distribution of the misorientation gradient for ⟨111⟩//ND and ⟨001⟩//ND grains separately is shown in Fig. 4. Comparing the accumulative frequency for ⟨111⟩//ND grains (Fig. 4a) to ⟨001⟩//ND grains (Fig. 4b) it can be observed that there is a shift to lower misorientation gradient values for ⟨001⟩//ND grains. The

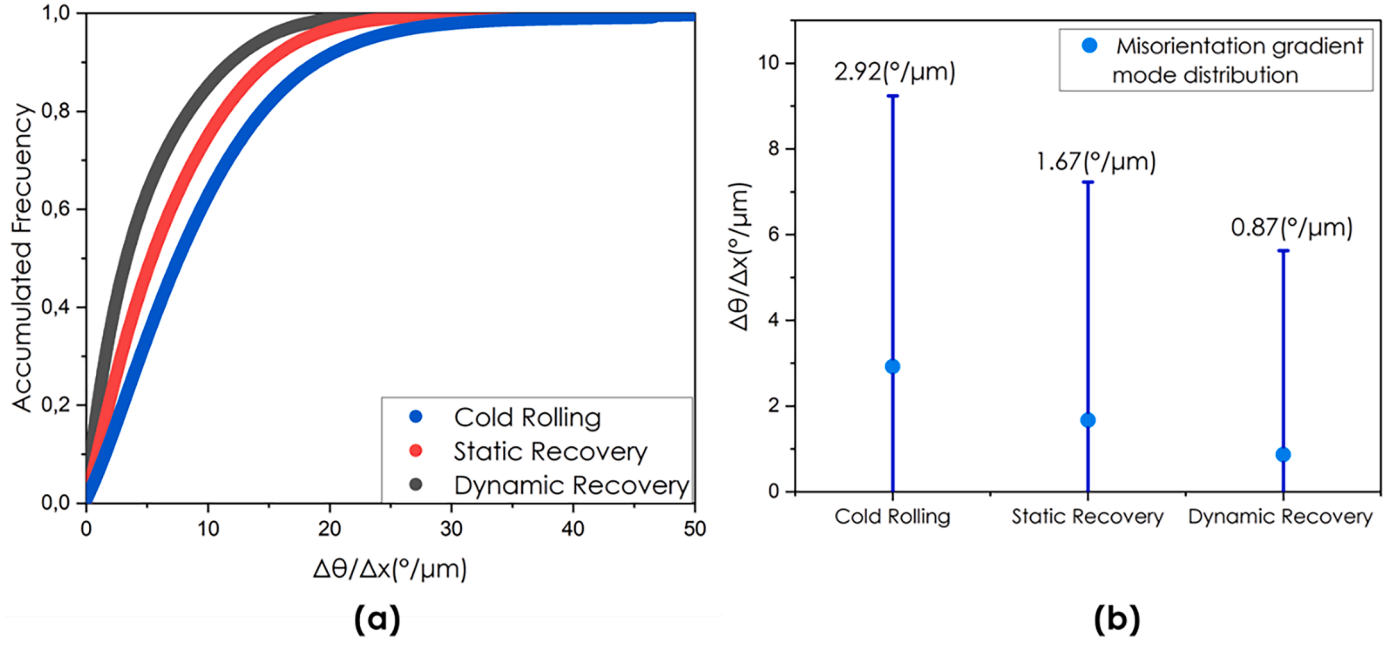

Fig. 3. (a) Accumulated frequency distribution of misorientation gradient derived from EBSD scan with step size 0.1 μm for three considered states and (b) Misorientation gradient distribution mode and standard deviation of the distribution.

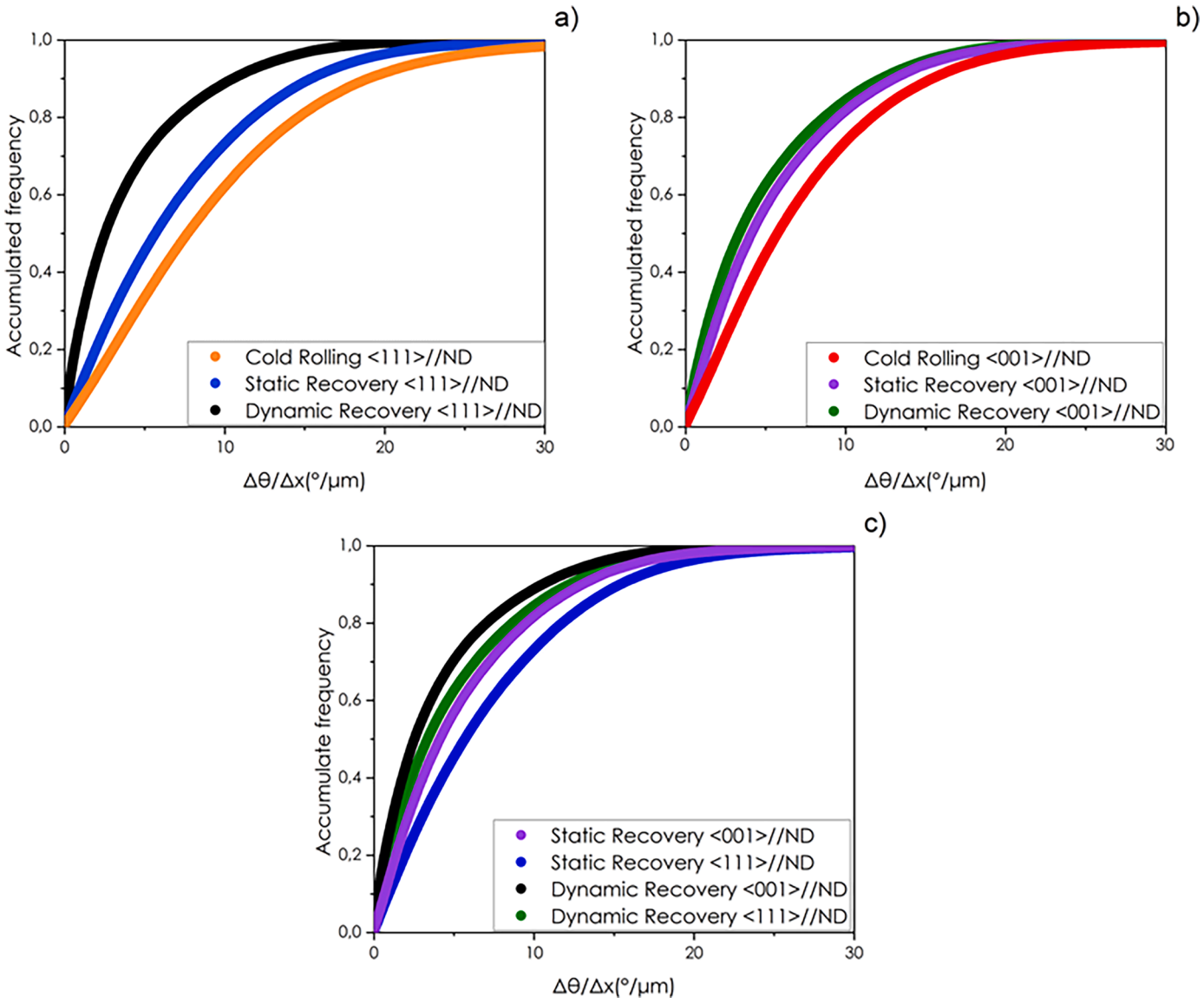

Fig. 4. (a) Accumulated frequency distribution of the misorientation gradient for ⟨111⟩//ND orientations; (b) ⟨001⟩//ND orientations in 3 considered conditions and (c) grains ⟨111⟩//ND and ⟨001⟩//ND static and dynamic recovery.

Fig. 4c gradient exhibits a shift to lower values for ⟨001⟩//ND grains compared to ⟨111⟩//ND grains. The misorientation shifts to lower values of the misorientation gradient in the dynamically recovered state and with similar behavior but to a lesser degree for the static recovery.

During warm rolling at ~550 °C short-range interactions are more readily overcome by thermal activation, allowing for increased dislocation mobility. The thermal factor in dynamic recovery causes subgrain boundary structures to migrate, merge with neighbors, reconfigure, or decompose [38]. Table 2 and Fig. 4 show that both ⟨111⟩//ND and ⟨001⟩//ND grains are equally sensitive to changes in the recovery kinetics, but the consequences for subsequent nucleation of ⟨111⟩//ND grains during static nucleation might be more important, as discussed below. Evidence of different recovery kinetics in ⟨111⟩//ND grains can be seen in the TKD image of Fig. 5. The analysis focuses on ⟨111⟩//ND grains because of the relevance of these orientations for the orientation selection during recrystallization after cold rolling. The key difference between the statically and dynamically recovered ⟨111⟩//ND grains is the presence or absence, respectively, of short-range orientation gradients, which prevents them from nucleation after warm rolling as it is known that short-range orientation gradients are instrumental in enhancing nucleation [39]. The TKD scans reveal the presence of a more pronounced remnant LAGB structure with increased misorientations after static recovery (Fig. 5a) as compared to the dynamically recovered stated (Fig. 5b).

It may be surmised that the essential difference between static and dynamic recovery is related to the activation energy. In dynamic recovery, this energy remains constant throughout progressive recovery, maintaining a steady dislocation balance under flow stress. Conversely, in static recovery, the activation energy decreases due to the consumption of recovery sites. Furthermore, the diffusion rate for eliminating dipoles in static recovery is considerably lower than in dynamic recovery as dislocation mobility is not mechanically enhanced, resulting in a slower kinetic process [11].

The present findings are relevant for the formation of the static recrystallization texture after cold vs. warm rolling. It is well-known that the thermodynamic and kinetic instabilities play a crucial role in the early nucleation stage at the onset of recrystallization [17,40–42] and that these are largely controlled by short-range orientation gradients [39,43–46]. The present results show that in the dynamically recovered condition after warm rolling, the local orientation gradients are significantly reduced compared to the statically recovered state. This plays a crucial role particularly for intra-grain nucleation in ⟨111⟩//ND

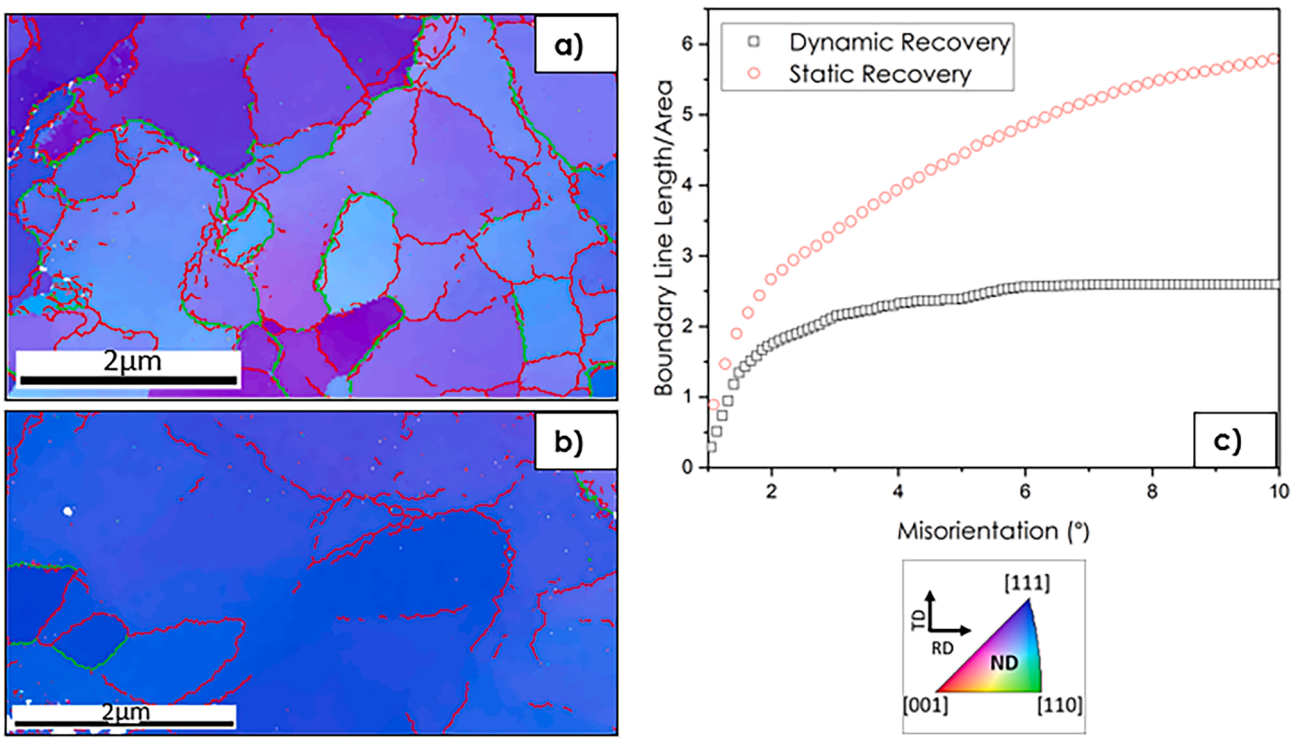

Fig. 5. Transmission Kikuchi Diffraction (a) ⟨111⟩//ND IPF map after static recovery (b) ⟨111⟩//ND IPF map of the dynamically recovered sample, green color 5°−10°, and red color 1°−5° misorientation (c) boundary density in static and dynamic recovery, step size 15 nm.

deformation bands in warm rolled material as it is very much likely to reduce the nucleation frequency of these orientations by lack of short-range orientation gradients. Alternatively, the ⟨001⟩//ND grains still maintain the potency to bulge into the ⟨111⟩//ND grains [39]. Hence the different types of substructures between warm and cold rolled sheets, though exhibiting similar deformation textures, may give rise to a different texture formation during subsequent static recrystallization.

CRediT authorship contribution statement

Estefanía Sepúlveda Hernández: Writing – review & editing, Writing – original draft, Visualization, Validation, Software, Resources, Project administration, Methodology, Investigation, Funding acquisition, Data curation, Conceptualization. **Tuan Nguyen-Minh:** Writing – review & editing, Writing – original draft, Supervision, Methodology, Conceptualization. **Konstantina Traka:** Writing – review & editing, Methodology, Formal analysis. **Felipe Castro Cerda:** Supervision, Funding acquisition. **Leo A.I. Kestens:** Writing – review & editing, Writing – original draft, Validation, Supervision, Methodology, Investigation, Formal analysis, Conceptualization.

Declaration of competing interest

The authors declare that they have no known competing financial interests or personal relationships that could have appeared to influence the work reported in this paper.

Acknowledgments

E.A. Sepulveda Hernandez acknowledges the support of the National Agency for Research and Development (ANID-Chile)/Doctorado Nacional/2021– 21210158.

References

[1] J.M. Burgers, Geometrical considerations concerning the structural irregularities to be assumed in a crystal, Proc. Phys. Soc. 52 (1940), https://doi.org/10.1088/0959-5309/52/1/304.
[2] S.Eswarappa Prameela, T.P. Weihs, A defect determines strength, Nat. Phys. 16 (2020), https://doi.org/10.1038/s41567-020-0961-2.
[3] G.I. Taylor, Plastic strain in metals, Twenty-Eighth May Lecture to the Institute of Metals (1938).
[4] M.R. Barnett, J.J. Jonas, Influence of ferrite rolling temperature on grain size and texture in annealed low C and IF steels, ISIJ Int. 37 (1997), https://doi.org/10.2355/isijinternational.37.706.
[5] M.R. Barnett, J.J. Jonas, Influence of ferrite rolling temperature on microstructure and texture in deformed low C and IF steels, ISIJ Int. 37 (1997), https://doi.org/10.2355/isijinternational.37.697.
[6] M.R. Barnett, Role of in-grain shear bands in the nucleation of ⟨111⟩ //ND recrystallization textures in warm rolled steel, ISIJ Int. 38 (1998), https://doi.org/10.2355/isijinternational.38.78.
[7] W.B. Hutchinson, Deformation substructures and recrystallisation, Mater. Sci. Forum (2007) 558–559, https://doi.org/10.4028/www.scientific.net/msf.558-559.13.
[8] M. Atake, M. Barnett, B. Hutchinson, K. Ushioda, Warm deformation and annealing behaviour of iron-silicon-(carbon) steel sheets, Acta Mater. (2015) 96, https://doi.org/10.1016/j.actamat.2015.05.018.
[9] W.B. Hutchinson, Development and control of annealing textures in low-carbon steels, Int. Metals Rev. 29 (1984), https://doi.org/10.1179/imtr.1984.29.1.25.
[10] B. Hutchinson, Deformation microstructures and textures in steels, Philos. Trans. R. Soc., A 357 (1999), https://doi.org/10.1098/rsta.1999.0385.
[11] U.F. Kocks, H. Mecking, Physics and phenomenology of strain hardening: the FCC case, Prog. Mater Sci. 48 (2003), https://doi.org/10.1016/S0079-6425(02)00003-8.
[12] Multiscale phenomena in plasticity: from experiments to phenomenology, Model. Mater. Eng. (2000), https://doi.org/10.1007/978-94-011-4048-5.
[13] G. Gottstein, Physical Foundations of Materials Science, 2004. https://doi.org/10.1007/978-3-662-09291-0.
[14] M.R. Gilbert, S. Queyreau, J. Marian, Stress and temperature dependence of screw dislocation mobility in α-Fe by molecular dynamics, Phys. Rev. B Condens. Matter. Mater. Phys. 84 (2011), https://doi.org/10.1103/PhysRevB.84.174103.
[15] E. Nes, Recovery revisited, Acta Metall. Mater. 43 (1995), https://doi.org/10.1016/0956-7151(94)00409-9.
[16] J.C.M. Li, Dislocation dynamics in deformation and recovery, Can. J. Phys. 45 (1967), https://doi.org/10.1139/p67-043.
[17] F.J. Humphreys, G.S. Rohrer, A. Rollett, Recrystallization and Related Annealing Phenomena, 3rd Edition, 2017.
[18] J. Mayer, L.A. Giannuzzi, T. Kamino, J. Michael, TEM sample preparation and FIB-induced damage, MRS Bull. 32 (2007), https://doi.org/10.1557/mrs2007.63.

[19] O.I.M. EDAX, Analysis Help, ChartChart (2013).
[20] F. Cruz-Gandarilla, R.E. Bolmaro, H.F. Mendoza-León, A.M. Salcedo-Garrido, J. G. Cabañas-Moreno, Study of recovery and first recrystallisation kinetics in CGO Fe3%Si steels using misorientation-derived parameters (EBSD), J. Microsc. (2019) 275, https://doi.org/10.1111/jmi.12822.
[21] S.I. Wright, M.M. Nowell, D.P. Field, A review of strain analysis using electron backscatter diffraction, Microsc. Microanal. 17 (2011), https://doi.org/10.1017/S1431927611000055.
[22] L.N. Brewer, D.P. Field, C.C. Merriman, Mapping and assessing plastic deformation using EBSD. Electron Backscatter Diffraction in Materials Science, SpringerLink, 2009, https://doi.org/10.1007/978-0-387-88136-2_18.
[23] C. Moussa, M. Bernacki, R. Besnard, N. Bozzolo, Statistical analysis of dislocations and dislocation boundaries from EBSD data, Ultramicroscopy (2017) 179, https://doi.org/10.1016/j.ultramic.2017.04.005.
[24] C. Moussa, M. Bernacki, R. Besnard, N. Bozzolo, About quantitative EBSD analysis of deformation and recovery substructures in pure Tantalum, in: Proc. IOP Conf. Ser. Mater. Sci. Eng., 2015, https://doi.org/10.1088/1757-899X/89/1/012038.
[25] H. Lanjewar, S. Naghdy, P. Verleysen, L.A.I. Kestens, Statistical analysis of dislocation substructure in commercially pure aluminum subjected to static and dynamic high pressure torsion, Mater. Charact. 160 (2020), https://doi.org/10.1016/j.matchar.2019.110088.
[26] W. Pantleon, Resolving the geometrically necessary dislocation content by conventional electron backscattering diffraction, Scr. Mater. 58 (2008), https://doi.org/10.1016/j.scriptamat.2008.01.050.
[27] P.J. Konijnenberg, S. Zaefferer, D. Raabe, Assessment of geometrically necessary dislocation levels derived by 3D EBSD, Acta Mater. (2015) 99, https://doi.org/10.1016/j.actamat.2015.06.051.
[28] A.J. Schwartz, M. Kumar, B.L. Adams, D.P. Field, Electron backscatter diffraction in materials science, 2009. https://doi.org/10.1007/978-0-387-88136-2.
[29] M. Kuwahara, K. Hachimura, S. Eiho, M. Kinoshita, Processing of RI-angiocardiographic images, in: Proceedings of the Digital Processing of Biomedical Images, 1976, https://doi.org/10.1007/978-1-4684-0769-3_13.
[30] A. Ayad, M. Ramoul, A.D. Rollett, F. Wagner, Quantifying primary recrystallization from EBSD maps of partially recrystallized states of an IF steel, Mater. Charact. 171 (2021), https://doi.org/10.1016/j.matchar.2020.110773.
[31] H. Mirzadeh, J.M. Cabrera, A. Najafizadeh, P.R. Calvillo, EBSD study of a hot deformed austenitic stainless steel, Mater. Sci. Eng. A 538 (2012), https://doi.org/10.1016/j.msea.2012.01.037.
[32] M.H. Alvi, S.W. Cheong, J.P. Suni, H. Weiland, A.D. Rollett, Cube texture in hot-rolled aluminum alloy 1050 (AA1050)-nucleation and growth behavior, Acta Mater. 56 (2008), https://doi.org/10.1016/j.actamat.2008.02.037.
[33] S.H. Hong, D.N. Lee, Recrystallization textures in cold-rolled Ti bearing IF steel sheets, ISIJ Int. 42 (2002), https://doi.org/10.2355/isijinternational.42.1278.
[34] G. Cai, C. Li, B. Cai, Q. Wang, Effects of warm rolling reduction on the microstructure, texture and magnetic properties of Fe-6.5 wt% Si steel, J. Mater. Res. (2016) 31, https://doi.org/10.1557/jmr.2016.179.
[35] M.R. Barnett, J.J. Jonas, Distinctive aspects of the physical metallurgy of warm rolling, ISIJ Int. 39 (1999), https://doi.org/10.2355/isijinternational.39.856.
[36] T. Furu, R. Ørsund, E. Nes, Subgrain growth in heavily deformed aluminium-experimental investigation and modelling treatment, Acta Metall. Mater. 43 (1995), https://doi.org/10.1016/0956-7151(94)00410-2.
[37] J. Gil Sevillano, P. van Houtte, E. Aernoudt, Large strain work hardening and textures, Prog. Mater Sci. 25 (1980), https://doi.org/10.1016/0079-6425(80)90001-8.
[38] H.J. McQueen, The production and utility of recovered dislocation substructures, Metall. Trans. A 8 (1977), https://doi.org/10.1007/BF02661562.
[39] K. Traka, K. Sedighiani, C. Bos, J. Galan Lopez, K. Angenendt, D. Raabe, J. Sietsma, Topological aspects responsible for recrystallization evolution in an IF-steel sheet – Investigation with cellular-automaton simulations, Comput. Mater. Sci. 198 (2021), https://doi.org/10.1016/j.commatsci.2021.110643.
[40] R.D. Doherty, D.A. Hughes, F.J. Humphreys, J.J. Jonas, D. Juul Jensen, M. E. Kassner, W.E. King, T.R. McNelley, H.J. McQueen, A.D. Rollett, Current issues in recrystallization: a review, Mater. Sci. Eng. A 238 (1997) 219–274, https://doi.org/10.1016/S0921-5093(97)00424-3.
[41] P.R. Rios, F. Siciliano, H.R.Z. Sandim, R.L. Plaut, A.F. Padilha, Nucleation and growth during recrystallization, Mater. Res. 8 (2005) 225–238, https://doi.org/10.1590/S1516-14392005000300002.
[42] D. Raabe, Recovery and recrystallization: phenomena, physics, models, simulation, in: physical metallurgy: fifth edition, Elsevier Inc. (2014) 2291–2397, https://doi.org/10.1016/B978-0-444-53770-6.00023-X.
[43] R.W. Cahn, A new theory of recrystallization nuclei, Proc. Phys. Soc. London Sect. A 63 (1950), https://doi.org/10.1088/0370-1298/63/4/302.
[44] P.A. Beck, The formation of recrystallization nuclei [6], J. Appl. Phys. 20 (1949), https://doi.org/10.1063/1.1698446.
[45] J.L. Walter, E.F. Koch, Substructures and recrystallization of deformed (100)[001]-oriented crystals of high-purity silicon-iron, Acta Metall. 11 (1963), https://doi.org/10.1016/0001-6160(63)90062-2.
[46] E.A. Holm, M.A. Miodownik, A.D. Rollett, On abnormal subgrain growth and the origin of recrystallization nuclei, Acta Mater. (2003) 51, https://doi.org/10.1016/S1359-6454(03)00079-X.